Research

Microscopic and macroscopic assessment of carbonate dissolution for geologic CO_2 storage

Jacquelin E. Cobos[1] · Olav P. Folkvord[1] · Erik G. Søgaard[2] · Bergit Brattekås[1]

Abstract

Carbon capture and storage in underground formations might be considered as a relevant technology to curb anthropogenic climate gas emissions. However, carbon dioxide (CO_2) injection can lead to severe rock-fluid interactions depending on the thermodynamic conditions, rock and fluids composition. The progressive dissolution of CO_2 in the formation brine results in mineral dissolution/precipitation processes that may drastically change the properties of the reservoir. This study is an attempt to get a deeper understanding of the dissolution/precipitation processes in a heterogeneous limestone at microscopic and macroscopic levels by a synergy between Isothermal Titration Calorimetry (ITC) and core flooding experiments with in-situ imaging to quantify uneven displacement fronts and understand the influence of reactions on a larger scale. Rock-fluid and fluid-fluid interactions, evaluated by ITC experiments, indicate that the carbonate dissolution is unfavorable with respect to enthalpy change but thermodynamically favorable with respect to entropy change (cations and hydrogen carbonate increase in the brine). Core flooding experiments with in-situ imaging by PET/CT show that complex pore structures cause a variation in the availability and ratio of the reactive fluid throughout the porous medium, hence, non-uniform dissolution was confirmed at core scale. The synergy between microcalorimetry and core flooding provides relevant insights into the dissolution of heterogeneous carbonate rocks at both microscopic and macroscopic scales.

Abbreviations

ϕ	Porosity
BPR	Backpressure regulator
CCS	Carbon capture and storage
d	Diameter
f_g	Gas fraction
ITC	Isothermal titration calorimetry
k_0	Initial permeability
k	Post-dissolution permeability
l	Length

✉ Jacquelin E. Cobos, jacquelin.e.mora@uib.no | [1]Department of Physics and Technology, University of Bergen, Bergen, Norway. [2]Department of Chemistry and Bioscience, Aalborg University, Copenhagen, Denmark.

P	Pressure
PV	Pore volume
PVI	Pore volumes injected
Q	Injection rate
T	Temperature
l-CO_2	Liquid CO_2
sc-CO_2	Supercritical CO_2

1 Introduction

CO_2 emissions are an inevitable side effect of human activities, such as burning fossil fuels/biomass, and certain chemical reactions (e.g. cement production) [1]. Hence, CO_2 emissions have risen steadily in the last 170 years, deviating from its cyclic variation before the industrial revolution [2]. The accumulation of CO_2 and other greenhouse gases (e.g. methane, nitrous oxides and fluorinated gases) produces a change in the Earth's energy balance, which results in either warming or cooling effects over time [3].

The recognition of the climate change effects on the environment drives the implementation of measures to reduce the CO_2 emissions, aiming to limit the temperature increase to 1.5 °C above pre-industrial levels [2, 4]. A widely accepted solution to reduce greenhouse gas emissions is carbon capture and storage (CCS): capturing CO_2 from large industrial point sources with subsequent permanent storage in appropriate geological formations, such as depleted oil and gas reservoirs, unminable coal beds, and deep saline aquifers [1, 5]. Among the available geological formations, depleted oil and gas reservoirs may be the best options for underground CO_2 storage because of the existence of infrastructure, wealth of data, and potential revenue from incremental oil recovery [6, 7]. Carbonate reservoirs hold more than 50% of the known petroleum reserves worldwide [8, 9] and may, hence, be candidates of CO_2 storage through CO_2-EOR. Injected CO_2 dissolving in formation brine, however, forms carbonic acid (H_2CO_3) and dissolution of carbonate rock is a direct consequence of this weak acidic environment. Dissolution changes the rock properties (porosity and permeability) over time, and could alter the performance of carbonate CO_2 storage reservoirs [10].

Understanding CO_2-induced dissolution process is relevant to safely utilize carbonate reservoirs for geological CO_2 sequestration and storage. Several reactions may occur within a ternary system composed of water, CO_2, and calcite ($CaCO_3$) that determine the carbonate dissolution and precipitation [11, 12]. Summarized controlling reactions are shown in Supplementary Material A. When the solution is supersaturated with respect to its dissolved constituents, $CaCO_3$ will precipitate from solution due to its low solubility. The resulting precipitates can reduce the permeability of the carbonate rock by 1) deposition on the pore walls due to attractive forces, 2) pore throats blocking, and 3) particle bridging across a pore throats [13]. Coto et al. [14] simulated the influence of temperature, pressure, pH, and ionic strength on $CaCO_3$ solubility using a thermodynamic model and found that solubility was inversely proportional to temperature and proportional to pressure. Coto and co-authors [14] further found $CaCO_3$ solubility to be inversely proportional to pH and proportional to ionic strength, reaching a maximum at a ionic strength similar to seawater.

Dissolution patterns are influenced by several factors, such as reaction kinetics, chemical interactions between fluids and solids (CO_2-brine-reservoir rock), rock heterogeneities, temperature, and pressure [13, 15–17]. Different experimental approaches have been used to study dissolution phenomena. The present study aims to gain insights into CO_2-induced dissolution of heterogeneous carbonate rocks using a synergy between microcalorimetry and core flooding experiments. To our knowledge, CO_2-brine-reservoir rock interactions have not been studied by microcalorimetry. This work provides the first microcalorimetric measurements and utilizes coreflooding experiments with current in-situ imaging methodologies to understand the influence of reactions on a larger scale. Hence, providing relevant insights into the dissolution of carbonate rocks at both microscopic and macroscopic levels.

2 Materials and methods

2.1 Fluids

Synthetic North Sea formation brine (NFB) and 3.5 wt% NaCl brine were prepared by mixing distilled water with reagent grade salts (purity of 99%, provided by VWR chemicals). Note that 0.01 wt% sodium azide (NaN_3) was added to the brines

Table 1 Ionic composition in mmol/l and intrinsic properties of synthetic North Sea formation brine (NFB) and 3.5 wt% NaCl brine. Ionic strength (I_c) in mmol/l, density (ρ) in g/cm^3 at 20°C. Brine pH was measured to 5.6. The density of NFB and NaCl brines was measured at ambient temperature (20 °C) with DMA 35 Anton Paar portable density meter apparatus (reproducibility of 0.0005 g/cm^3)

	Ionic composition							Intrinsic properties	
	K^+	Mg^{2+}	Na^+	Ca^{2+}	SO_4^{2-}	Cl^-	HCO_3^-	Ic	ρ
NFB	4.7	21.89	995.96	99.92	0.7	1064.56	8.92	1.28	1.06
NaCl	–	–	684.40	–	–	684.40	–	0.68	1.05

The ionic concentrations of the synthetic brines were determined by the general dissociation theory based on the molecular weight of the salts and the amount of mass added to the solution [19]. The ionic strength was estimated based on the ionic concentration and the charge of each ion

Table 2 Physical properties of CO_2

	Density [g/ml]		Viscosity [cP]	
	20°C, 9 MPa	40°C, 9 MPa	20°C, 9 MPa	40°C, 9 MPa
CO_2	0.84 [a]	0.49 [b]	0.08 [a]	0.03 [b]

[a] liquid

[b] supercritical conditions [20]

Table 3 X-ray Fluorescence (XRF) analysis of Edwards Limestone

	Compound						
	Si	S	K	Ca	Fe	As	Sr
Mass %	0.55	0.02	0.07	98.7	0.38	0.20	0.08

Particles with a size of < 100 μm, obtained by crushing and grounding part of the rock material with a ball mill

Table 4 Core properties and overview of experiments

Core properties						Experimental conditions					
Core id	l [cm]	d [cm]	ϕ %	k_o [mD]	k [mD]	PV [ml]	P [MPa]	T [C]	Q [ml/h]	PVI [ml]	
E-1	7.4	3.8	20.8	39.9	17.7	17.4	9	40	72	400	Continuous sc-CO_2/NaCl and brine injections
E-2	7.4	3.8	22.8	54.7	46.6	19.1	9	25	72	409	Continuous l-CO_2/NaCl and brine injections
E-3	7.6	3.8	23.1	42.6	20.8	20.9	9	40	72	168	Discontinuous sc-CO_2/NaCl and brine injections
E-4	7.5	3.8	22.2	48.0	55.0	18.9	9	25	48	175	Discontinuous l-CO_2/NaCl and brine injections

to prevent bacterial growth [18]. Ultra-pure water (UPW) for high performance liquid chromatography (HPLC) was used for baseline ITC experiments. The fluids were saturated with CO_2 at ambient conditions using a mass flow controller at a rate of 120 ml/h for 30 min. Ionic composition, ionic strength, and intrinsic properties for both brines are shown in Table 1.

The physical properties of CO_2 with a purity of 99.99 % are presented for the experimental conditions in Table 2.

2.2 Rock material

Edwards Limestone is a heterogeneous carbonate from the Early Cretaceous period, exhibiting a trimodal pore size distribution with both vugs and microporosity [21]. Four cylindrical core samples (diameter 3.8 cm, Table 4) were used for dynamic dissolution and imaging experiments at Darcy scale in this study. The core samples were clearly heterogeneous with visible vugs, and pore sizes ranging from 29 to 3317 μm measured by micro-CT (μCT) [21]. Grinded core material was also used for microcalometric scale experiments.

The elemental composition of the rock material was found using X-ray Fluorescence (XRF) and X-ray Power Diffraction (XRD) analysis. XRF (Table 3) and XRD (Supplementary Material B) showed that Edwards Limestone mainly consisted of calcite (98.7 %)

The cores were washed gently with tap water to remove debris and lose particles, in preparation for the CO_2 and brine co-injection. Dry weights and dimensions of each core were registered after drying for 2 weeks in a heating cabinet at 60°C. The effective porosity was determined gravimetrically by air evacuating and saturating the cores with NFB [22], and absolute brine permeability was calculated using Darcy's law by measuring the pressure drop across the core samples during water injection at different flow rates (50 ml/h, 100 ml/h, 150 ml/h, and 200 ml/h). Edwards Limestone core properties and experimental conditions applied during core floods are presented in Table 4.

2.3 Microcalorimetry procedures

A multichannel microcalorimetric system from TA Instruments, TAM IV, was used to get a deeper insight into the calcite dissolution at microscopic level. Isothermal Titration Calorimetry (ITC) gives a direct appraisal of the thermodynamics behind complex bio-, physico-, chemical and geological processes by measuring the heat absorbed or released [23]. A graphical representation of the microcalorimetric system and carbonate dissolution/precipitation at microscopic scale can be found in Fig 1.

ITC experiments were performed using ampules containing a slurry of 100 mg Edwards Limestone and 200 μL NFB at a temperature of 40 °C and ambient pressure. Seven injections of 9.948 μL NaCl brine saturated with CO_2 (B_{CO_2}) were titrated separately into the limestone+NFB system. The interval time between injections was 420 s. The ITC main limitation is that it can only be run at ambient pressure and a known temperature. However, Gibbs free energy (ΔG) of chemical reaction is independent of pressure. Consequently, the point of equilibrium will be the same at 1 and 9 MPa, hence, ITC experiments are comparable with the corefloods. Note that a new calibration of the microcalorimeter is required every time that the temperature is modified.

ITC of fluid-fluid interactions (B_{CO_2} into NFB) were also performed without rock particles: 200 μl of NFB was placed into the ampule and 7 injections of 9.948 μL of B_{CO_2} were carried out with 420 s time intervals. Direct limestone+B_{CO_2} interaction was measured by placing 100 mg of the rock sample in the ampule and then adding B_{CO_2}.

The effect of CO_2 in rock-fluid-fluid and fluid-fluid interactions was determined by four blank experiments. In two experiments, 3.5 wt% NaCl without CO_2 was used to determine the effect of CO_2 in rock-fluid-fluid and fluid-fluid interactions. Ultra-pure water (UPW) with or without CO_2 was used with limestone+NFB system in the remaining two experiments to isolate rock dissolution from other effects (e.g. presence of ionic species). Table 5 presents a summary of the microcalorimetric experiments performed in this study. Note that the ITC experiments were analyzed using $NanoAnalyze^{TM}$ software from TA Instruments ([23–25]).
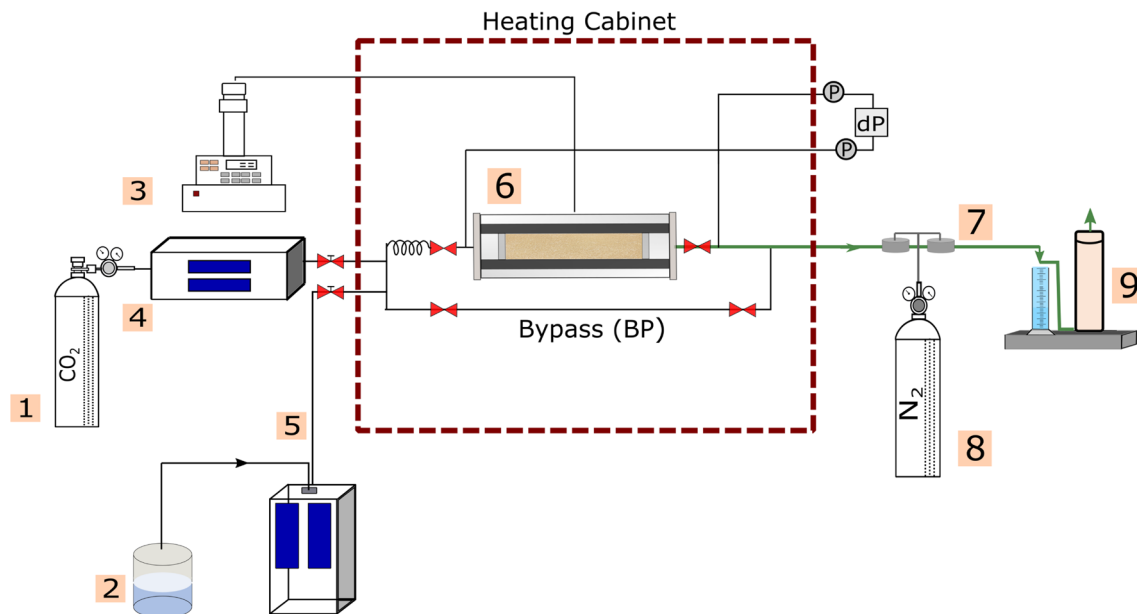
2.4 Dissolution experiments

Calcite dissolution was studied on the core scale during steady-state CO_2 and brine co-injection using the experimental setup presented in Fig. 2 and slightly different experimental procedures. The CO_2 fraction was kept constant at 80% of the total volume injected in all experiments, which decreased the co-injected phase pH to 4.3. System pressure was 9.0–9.3 MPa, and temperature either at ambient or slightly elevated conditions (40 °C), hence, CO_2 was

Fig. 1 Representation of microcalorimeter apparatus and carbonate dissolution/ precipitation upon CO_2/NaCl brine injection at microscopic scale. 1-TAM IV microcalorimeter at 40 °C, 2-titration ampule, 3-reaction vessel (1 ml), 4-injection cannula, 5-brine and rock particles, 6-stirrer (100 rev/min) and 7-reactions
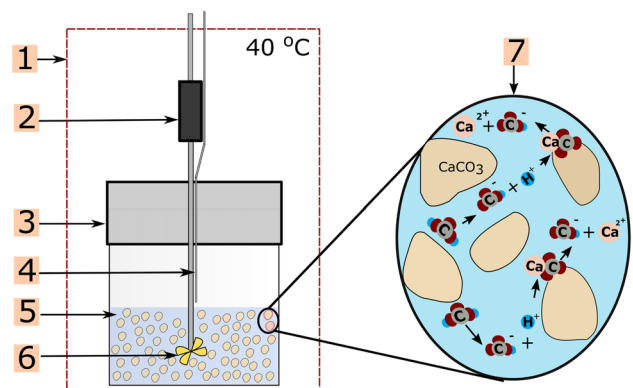
Table 5 Overview of microcalorimetry evaluation

| Interactions	Ampule	Titration		
		Fluid	Volume	Time injection
Rock-fluid-fluid	Limestone+NFB	B_{CO_2}	69.64	4800
Rock-fluid-fluid_blank	Limestone+NFB	B	69.64	4800
Rock-fluid-fluid_blank	Limestone+NFB	UPW	69.64	4800
Rock-fluid-fluid_blank	Limestone+NFB	UPW_{CO_2}	69.64	4800
Fluid-fluid	NFB	B_{CO_2}	69.64	4800
Fluid-fluid_blank	NFB	B	69.64	4800

Fig. 2 Experimental setup used during the calcite dissolution experiments: Each core was wrapped in aluminium foil to reduce CO_2 radial diffusion through the rubber sleeve of the core holder, and mounted horizontally within a heating cabinet. 1 - CO_2 bottle, 2 - Aqueous phase, 3 - Isco pump for confinement pressure, 4 - Quizix 6000–10k pump for CO_2 injection, 5 - Quizix 5000–10k pump for brine injection, 6 - Hassler-type core holder with core, 7 - Equilibar backpressure regulator, 8 - N_2 bottle, 9 - adsorption column and measuring cylinder. The confinement pressure was 10 bars above the system pressure at all times. The confinement and system pressures were increased gradually (10 bar at a time) to the experimental conditions during continuous brine injection, and a constant system pressure was maintained by two Equilibar backpressure regulators (BPR) connected to a nitrogen gas (N_2) tank. The first backpressure regulator ($\mathbf{BPR_1}$) was pressurized with approximately 3 bars above the second regulator ($\mathbf{BPR_2}$) to minimize pressure fluctuations in the system. Note that each fluid goes through a separate pneumatic valve before they are joined some distance before the inlet of the coreplug

in either liquid (l-CO_2) or supercritical (sc-CO_2) phase. Dynamic developments in differential pressure were recorded continuously before, during and after CO_2/NaCl brine co-injection and could indicate the creation (injection pressure reduction) or blockage (injection pressure increase) of flow paths in the porous medium. The differential pressure is not a direct indicator of dissolution: but provides dynamic monitoring of flow pattern changes in the core during injections. Cores E-1 and E-2 (4) were used to assess calcite continuous dissolution by monitoring the differential pressure during continuous steady-state co-injections. Cores E-3 and E-4 were used to assess dynamic core scale reactivity when two-phase CO_2/brine co-injections and single-phase NaCl brine injections were alternately injected over several days. E-4 injections were imaged using Positron Emission Tomography (PET)-Computed Tomography (CT) imaging. The temporal resolution of PET system is high compared to other imaging methods (seconds) and the spatial voxel size is 0.4 mm. The CT system has a resolution of 250x250x250 micron, and cannot capture pore size distributions for this core material, but provides access to larger heterogeneous features such as fractures. For additional details about the imaging system the reader is referred to Brattekås et al [26]. Multi-modal PET-CT was used to identify dynamic changes in core structure (CT) and fluid flow patterns (PET) due to dissolution of the core material. The experimental schedule of the 4 day long experiment may be found in Table 6.F^{18}-Fluorodeoxyglucose

Table 6 Overview of the injected fluids through E-4 coreplug

Day	Injected fluids
1	1.8PV F^{18}-FDG labelled brine
	1.4PV CO_2
	10.53PV two-phase injection (20% F^{18}-FDG labelled brine, 80% CO_2)
	NaCl brine injected until the next day
2	1.86PV F^{18}-FDG labelled brine
	21.90PV two-phase injection (20% F^{18}-FDG labelled brine, 80% CO_2)
	NaCl brine injected until the next day
3	1.6PV F^{18}-FDGlabelled brine
	20.2PV two-phase injection (20% F^{18}-FDG labelled brine, 80% CO_2)
	NaCl brine injected until the next day
4	2.92PV F^{18}-FDG labelled brine
	NaCl brine injected until the next day

Fig. 3 Heat flow vs time for limestone+NFB+B$_{CO_2}$ and limestone+NFB+B
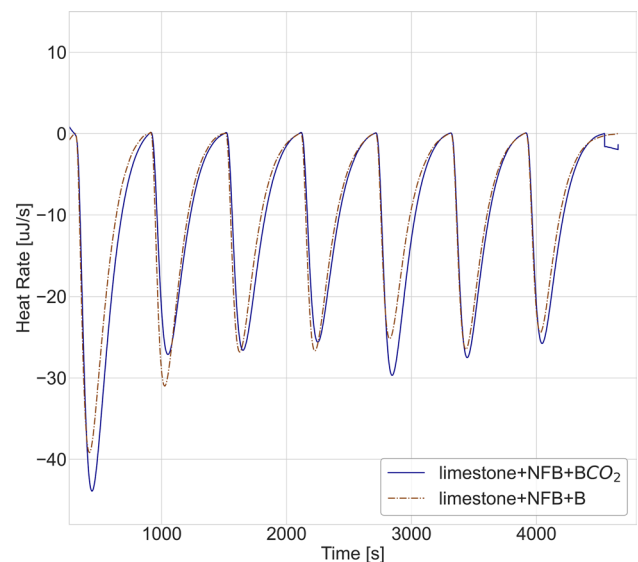
(F^{18}-FDG) radiotracer with a half-life of 109.7 min was used to label brine to render co-injections and pure brine injections detectable by PET.

3 Results and discussion

3.1 Dissolution at micro-scale

Rock-Fluid and Fluid-Fluid Interactions were measured on micro-scale using microcalometry. The raw heat signal registered by the microcalorimeter when B_{CO_2} or NaCl brine was injected into rock particle + NFB slurry is presented in Fig. 3. The peaks displayed in the thermograms for both systems indicate the addition of 9.947 μl of either B_{CO_2} or plain NaCl brine into the slurry. According to the data collection of the microcalorimeter ([23, 24, 27]), the heat flow signal shows an endothermic event when one of the fluids contact the rock+fluid system. The height of the endothermic peaks for both systems (Fig. 3) is higher at the initiation of the titration process, similar to previous observations with a salinity contrast ([27, 28]). As explained in Cobos et al. [29], the ionic strength difference between the injected fluid and the formation brine alters the equilibrium in the system. The microcalometric measurements (Fig. 3) shows that NaCl brine of a lower ionic strength interacts endothermically and dynamically with the rock and formation brine.

Table 7 Heat values for limestone+NFB+B_{CO_2} (system$_{1T}$) and limestone+NFB+B (system$_{2T}$)

	Injection no.						
	1	2	3	4	5	6	7
Heat$_{system1T}$ [mJ]	9.5±0.1	6.0±0.1	5.7±0.1	5.4±0.1	5.5±0.1	5.0±0.1	4.8±0.1
Heat$_{system2T}$ [mJ]	7.9±0.7	6.3±0.5	5.4±0.5	5.1±0.8	4.6±1.0	4.5±1.3	4.6±1.4

Fig. 4 Enthalpy change (ΔH) values for limestone+NFB+B_{CO_2} and limestone+NFB+B. An exception in ΔH can be observed for the second injection and might be related with artifacts during the heat flow measurements
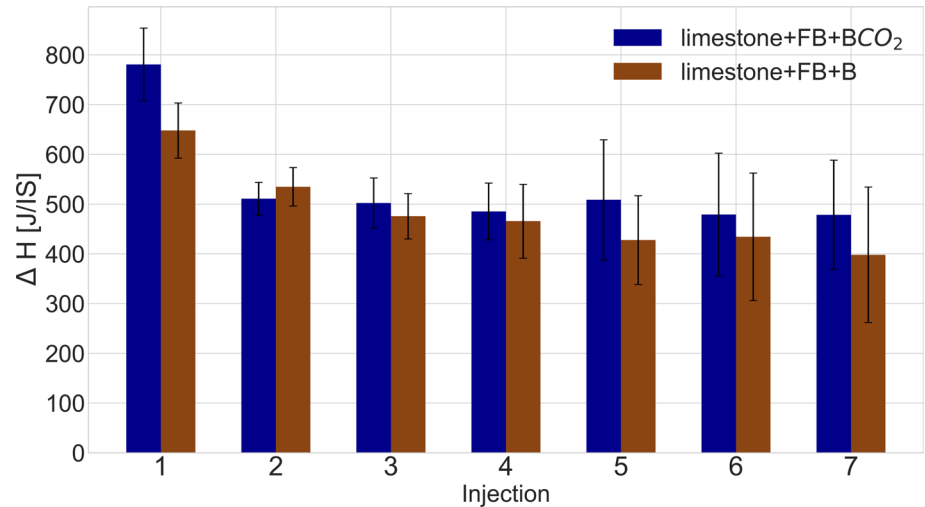
The heat developed (Q_{inj}) by each injection of $NaCl_{CO_2}$ or NaCl brine into Edwards Limestone particles can be obtained by integrating the heat rate displayed in Fig. 3 over time (Table 7). The heat absorbed by limestone+NFB+B_{CO_2} is higher than for limestone+NFB+NaCl brine, showing that CO_2 made the injected fluid more reactive with the rock+fluid system.

The enthalpy change per unit ionic strength (ΔH) for the total interaction can be determined by Eq. 1 based on the heat data presented in Table 7 [23]. In this equation, [IS] is the ionic strength of NaCl brine in mmol/L and V_i is the volume of each titration.

$$Q_{inj} = \left(\Delta H \times [IS] \times V_i \right)$$ (1)

Figure 4 shows the enthalpy change for the total interaction. The obtained ΔH values are higher for the injection of $NaCl_{CO_2}$ compared to plain NaCl into the limestone+NFB system, confirming that $NaCl_{CO_2}$ is more reactive than plain NaCl.

The thermograms for fluid-fluid interactions (injection of 3.5 wt% NaCl with and without CO_2 into formation brine) are presented in Fig. 5. The peaks for NFB+B_{CO_2} and NFB+NaCl brine are also endothermic, but smaller than rock-fluid-fluid measurements (Fig. 3). This could indicate that the total interaction in a system containing both rock and fluids is driven mainly by the presence of limestone particles. NFB+$NaCl_{CO_2}$ attains a higher heat flow than NFB+NaCl brine. The addition of a diluted fluid into a highly concentrated fluid requires energy from the system (dominantly endothermic) [28, 29] due to the mixing process that alters the hydrogen bonding between the water molecules (water-water network perturbation). The interaction between two fluids with a salinity contrast is more significant if CO_2 is dissolved in the injection fluid.

The obtained heat response from the rock+NFB+fluid system (Fig. 3) may be due to a rock dissolution process or the presence of ionic species (Na^+ and Cl^-) in the injected fluid. To reveal the primary mechanism, carbonated ultra pure water (UPW_{CO_2}) and ultra pure water (UPW) were injected separately into dried limestone particles saturated with NFB. The heat response obtained for the injection of UPW_{CO_2} and UPW is presented in Fig. 6.

Endothermic peaks were observed in the injection of ultra pure water with CO_2 into limestone (limestone+NFB+UPW_{CO_2}). This suggests that the endothermic peaks observed for limestone+NFB+$NaCl_{CO_2}$ is not connected to ionic species and, hence, are most likely caused by rock dissolution. According to Lasaga [30] and Golfier et al [31], calcite dissolution takes place in three steps: 1) transport of the reactants towards the surface, 2) reaction at the mineral surface, and 3) transport of reaction products away from the surface of reaction into the bulk solution. The latter increases the concentration of cations and hydrogen carbonate in the bulk solution which leads to changes in entropy as observed in Fig 1.

Fig. 5 Heat flow vs time for NFB+B$_{CO_2}$ and NFB+B without limestone particles
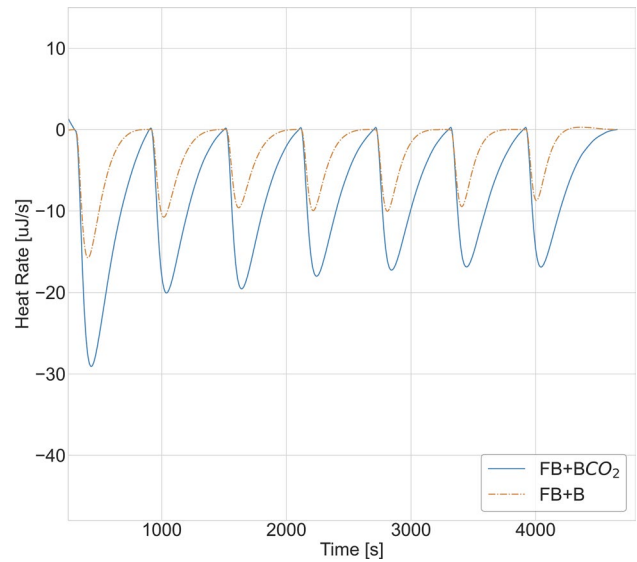
Fig. 6 Heat flow vs time for limestone+North Sea formation brine+ultra pure water$_{CO_2}$ and limestone+North Sea formation brine+ultra pure water. Note that the first exothermic peaks in both systems are associated with the alteration of the water-water network due to the salinity contrast between the injection and in-situ fluids
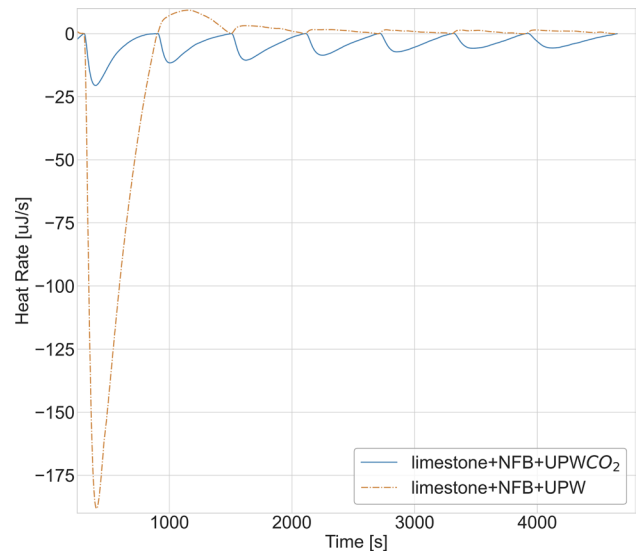
The injection of ultra-pure water without CO_2 into dried rock particles (Limestone+NFB+UPW) is mainly exothermic and could be associated with protonation and deprotonation reactions at the surface lattice. Coordination reactions with the solution species can go on at the protonated anion surface sites, $> CO_3H^0$ (Eq. 2), and at the hydroxylated cation sites, $> CaOH^0$, (Eqs. 3-4) of the calcium carbonate lattice [32–34].

$$> CO_3H^0 + OH^- \rightleftharpoons > CO_3^- + H_2O \tag{2}$$

$$> CaOH^0 + H^+ \rightleftharpoons > CaOH_2^+ \tag{3}$$

$$> CaOH^0 + OH^- \rightleftharpoons > CaO^- + H_2O \tag{4}$$

Table 8 shows the heat values for the injection of ultra pure water with CO_2 (UW_{CO_2}) and without CO_2 (UW) into Edwards Limestone. It is possible to obtain the direct effect of CO_2 on the rock lattice (Heat$_{CO_2-rock}$) by subtracting the protonation and deprotonation coordination reactions from the carbonated fluid (i.e. limestone+NFB+UW$_{CO_2}$ - limestone+NFB+UW = CO_2 effect.

Table 8 Heat values for limestone+UW$_{CO_2}$ and limestone+UW

inj	Heat$_{system1U}$	Heat$_{system2U}$	Heat$_{CO_2-rock}$
1	4.5±6.7	52.4±1.7	−48.0
2	2.9±0.5	−3.7±0.1	6.6
3	3.1±0.4	−1.2±0.1	4.3
4	2.6±0.1	−0.6±0.1	3.3
5	2.3±0.2	−0.5±0.1	2.8
6	2.0±0.2	−0.5±0.1	2.4
7	2.2±0.1	−0.6±0.1	2.8

The total heat (without taking into consideration the first peak due to evaporation effects) for UW$_{CO_2}$ is 14.7 mJ, UW − 5.9 mJ, and CO_2-rock 20.5 mJ. To the extent of our knowledge data sets about the enthalpy and entropy of the carbonate dissolution/precipitation processes (rock-fluid interactions upon CO_2 injection) have not previously been reported. Thermodynamics data sets have, however, been reported for sandstone rocks. Du and Leeuw [35] found, through molecular dynamics simulations, that the overall dissolution of a rock surface (α-quartz) in water is an endothermic process that requires energy to proceed (ΔH= 40 kJ/mol). The detachment of a silicon atom from the surface leads to an increase in entropy, which leads to the viability of the dissolution process in water. A similar process could have occurred for calcite, indicating that the dissolution process is unfavorable with respect to enthalpy change but thermodynamically favorable with respect to entropy change (cations and hydrogen carbonate increase in the brine).

The acquisition of interaction enthalpy values (ΔH) for the complex rock–fluid and fluid–brine systems and corefloods with in−situ imaging can help future CCS projects through the understanding of the dissolution and precipitation of the minerals and how they change under a wide range of operating conditions. The thermodynamics behind the rock–fluid and fluid–fluid interactions obtained by microcalorimetry is comparable to a larger scale (e.g. corefloods) because the Gibbs free energy (ΔG) of a chemical reaction is independent of pressure.

Core flooding experiments were further used to assess CO_2-brine-reservoir rock interactions, that were observed through microcalorimetry, on a larger scale.

3.2 Dissolution at darcy scale

3.2.1 Continuous single and multi-phase injections

The development in differential pressures during continuous co-injection of CO_2 and brine into core E-1 and E-2 is displayed in Fig. 7. The pressure increased during co-injection in both cores, indicating blockage of pores or flow paths due to dissolution and precipitation. The effluent pH increased above to 5.7, above initial brine pH, during co-injections which indicates calcite dissolution. Most of the injectivity change for CO_2 and brine co-injections at liquid and supercritical conditions occurred during the first 100 pore volumes injected (PVI), where the differential pressure increased linearly. This trend could be associated with the dissolution reaction kinetics: Cobos et al. [28] found that the dissolution of iron bearing carbonate cement by the injection of a brine with citric acid is also linear. Differential pressures in both core plugs stabilized after 100 PVI; some fluctuations were observed in E-2, as expected during two-phase flow. In E-1 three noticeable pressure declines of 10–15% were observed at 120 PVI, 240 PVI, 294 PVI and a slightly increasing trend continued throughout co-injection (400 PVI). Brine (without CO_2) was injected after co-injection, which resulted in an initial differential pressure spike that rapidly dropped before reaching a stable end-point. The change from two-phase to single-phase displacement in the coreplug causes this pressure development. Single-phase brine injection continued for 24 h to dissolve and displace all CO_2 from the core. The end point pressure showed a decrease in absolute permeability from 39.9 mD to 17.73 mD (E-1) and E-2 from 54.7 mD to 46.6 mD, i.e. an overall decrease in core permeability was observed for both cores after co-injection, likely related to dissolution and re-precipitation of particles within the pore network.

The differential pressure for E-2 (l-CO_2) is slightly higher than for E-1 (sc-CO_2) during co-injection. This could be because of a significant CO_2 density and viscosity difference between the experiments, caused by the different temperature conditions. A higher density means that more CO_2 moles are present at the liquid CO_2-brine interface and therefore also at the rock-liquid interface, which results in more significant dissolution of the rock minerals. Golfier et al. [31] found that the reactions at the calcite mineral surface occur very fast, and therefore its reactivity is transport-limited. This is in accordance with rotating-disc experiments done by Liu et al. [36] in which limestone dissolution was controlled by the
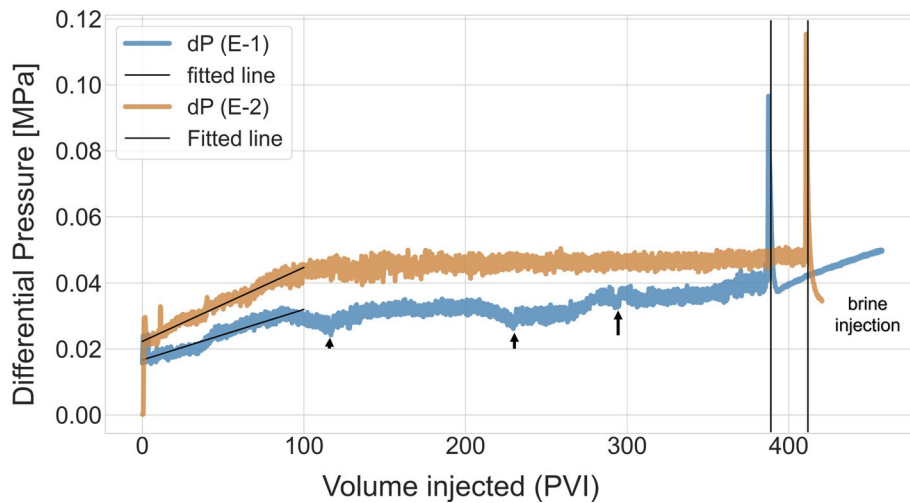
Fig. 7 Differential pressure (DP) development for E-1 (sc-CO_2) and E-2 (l-CO_2) coreplugs. Arrows in E-1 coreplug indicate pressure drops at 120 PVI, 240 PVI, 294 PVI, respectively. Single phase brine injection for E-1 is 0.028 MPa and post-dissolution brine injection is 0.035. DP end-point pre-dissolution brine injection for E-2 is 0.021 MPa and post-dissolution brine injection is 0.049. Brine injection results in a differential pressure spike that rapidly dropped before reaching the end-point differential pressure that might be caused by the displacement of CO_2 in the coreplug

mass transfer between the surface and the bulk solution, being sensitive to rotation speed (i.e. limestone dissolution increases with rotation speed).

3.2.2 Alternate single and multi-phase injections

Microcalorimetric measurements showed that rock reactivity decreased without CO_2 present in the rock-fluid system. Consequently, we designed two Darcy scale experiments where the reactive two-phase flow was alternated with single-phase brine injections. Four distinct periods of co-injection were followed by single-phase brine injections. Dynamic pressure developments during all floods, and in-situ imaging enabled insight into flow dynamics at the macroscopic scale during and between reactive flow. Differential pressure development over time can be found in Fig. 8 for core E-3 (CO_2 in supercritical phase).

The differential pressure dropped during the first co-injection period and was lower than single-phase brine injection pre-dissolution (DP=0.02 MPa). As expected, the shift to single-phase brine injection after 36 PVI of co-injection results in a swiftly increasing pressure which declined and stabilized at a higher value (DP=0.04 MPa). Any free-phase CO_2 in the pore space will dissolve into water and be displaced during 36 PVI of brine injected; hence, the pressure increase from

Fig. 8 Differential pressure development for E-3 during four consecutive co- and single phase- injections.The differential pressure during brine injection steadily increased from 0.02 MPa pre-dissolution to 0.039 MPa after four periods (168 PVI in total) of co-injection
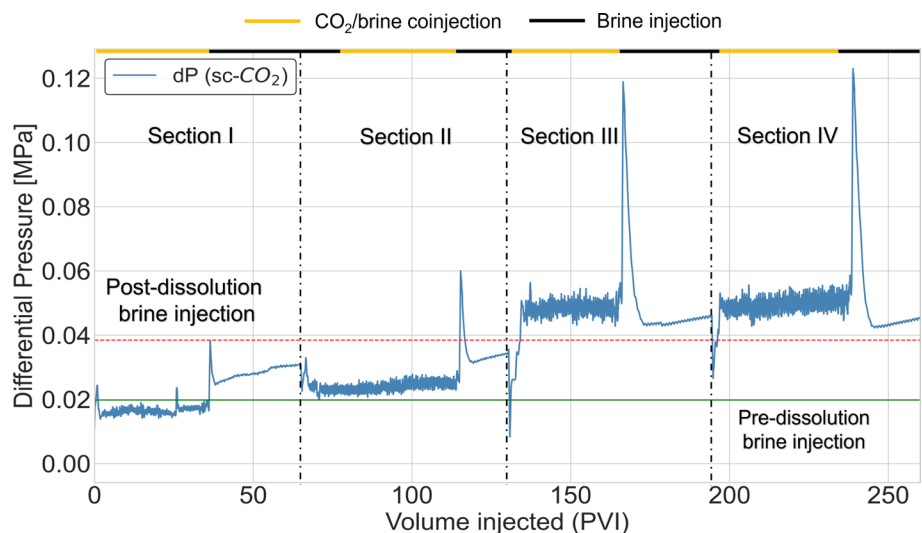
pre-dissolution level indicate a decrease in absolute permeability from 44.5 mD to 30.6 mD. The second period of sc-CO_2/brine co-injection initiated another pressure drop, after which the differential pressure remained stable slightly above pre-dissolution level. Minor fluctuations were observed, as expected, induced by two-phase flow. Second single-phase brine injection showed that core permeability had further decreased to 26.1 mD. The third and fourth co- and single phase- injections followed a similar trend, but exhibited a much higher pressure drop. The swift pressure increase at the initiation of the third co-injection could be related to a long shut-in time (12 days due to technical issues); however, the heat flow signal of the rock-fluid system quickly stabilizes without the presence of CO_2 (Fig. 3), which is not indicative of high reactivity and severe dissolution effects during shut-in. During brine injections, the displacement of CO_2 induces a differential pressure spike, which swiftly drops before reaching a lower end-point differential pressure. Brine injection was continued for 24 h after the fourth co-injection, and the final post-dissolution pressure (DP=0.039 MPa) corresponded to a core permeability of 22.9 mD.

The E-3 injections showed that core permeability decreased due to co-injection of CO_2 and brine, presumably caused by dissolution and precipitation within the pore space. *In-situ* imaging by PET/CT was further used to investigate changes in flow dynamics during alternate injections. PET imaging provides insight into the flow paths of traced brine, and was applied over several consecutive days during alternate co- and single phase-injections into E-4. To our knowledge this is the first experiment that applies PET imaging to dynamically visualize carbonate dissolution. The injection schedule can be found in Table 6 and the pressure development with time in Fig. 9. The experimental setup used was similar to the E−1, E−2 and E−3 core floods, but the core holder was custom made with floating end pieces [26]. A confinement pressure 15 Bars above the line pressure was maintained at all times to ensure fluid flow through core E−4. The main difference between E-3 and E-4 core floods was the temperature conditions: causing the E-4 injected CO_2 phase to be higher-density liquid. Continuous co-injection core floods in E-1 and E-2 confirmed that injection pressures were higher with CO_2 in the liquid phase. Brine injections were also performed over night for E-4 (due to constraints in the imaging lab) potentially giving the core more time to fully stabilize between co-injections; however, the injection rate was kept low to maintain comparison between the number of pore volumes injected in E-3 and E-4. The pressure development during three alternate co- and single phase- injections in E-4 is shown in Fig. 9. Similar observations as to E-1, E-2 and E-3 were made when the injection mode changed from two-phase to single-phase; a sharp pressure peak occurred, after which the pressure curve decreased. Small fluctuations in pressure were also observed during co-injections. The overall pressure development was, however, different: The differential pressure increased during co-injections, and was higher during the first period of co-injection compared to the second and third. The differential pressure during brine injections was lower than for co-injections, and decreased with time, indicating an increase in permeability for this core during time. The absolute core permeability increased from 48 to 55 mD due to CO_2 and brine displacement through the limestone core material: and the development in flow patterns was visualized and quantified by PET imaging.

Figure 10 shows the occupancy of F^{18}-FDG labelled brine in the pore volume during single-phase, miscible brine injections. Minute amounts (less than 0.5 ml) of F^{18}-FDG was used to label the injection brine (> 100 ml), and is not expected to influence the chemical or physical properties of the injected brine. The PET images explicitly show the injected, traced brine, not occupancy of CO_2. By comparing miscible injections over the course of several days, before and after consecutive exposures to CO_2 and brine co-injections, the influence of dissolution may, however, be visualized.

"Day 1" images show the displacement within E-4 pre-dissolution, i.e. before contact with CO_2. The properties of the injected and connate brine were similar, hence no heat exchange was expected between rock material and fluids

Fig. 9 Differential pressure (DP) development during injection of brine, CO_2, and CO_2-brine co-injection into E-4 coreplug. Pre-dissolution brine injection displayed with the dashed-green line and post-dissolution brine injection with red-solid line
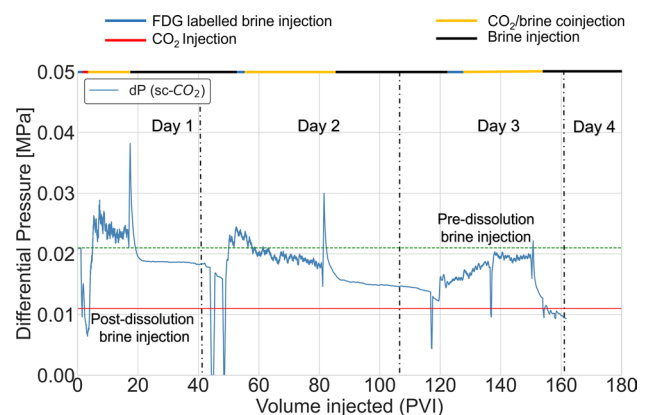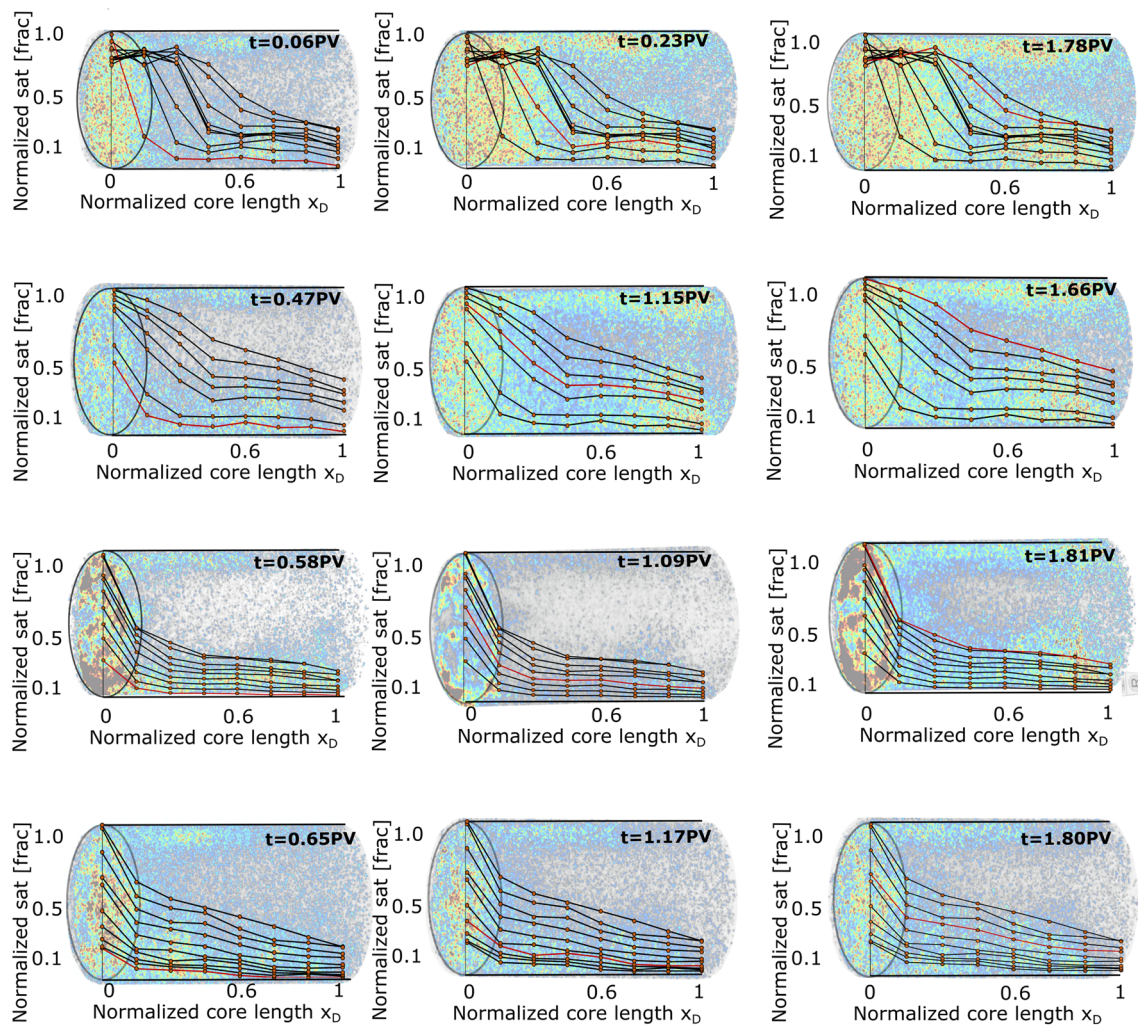
Fig. 10 Dynamic saturation development during F^{18}-FDG traced brine injection into E-4: 3D images are overlain by quantitative 1D saturation profiles. Warm colour in 3D images represent the highest PET signal intensity. Grey and white areas do not contain F^{18}-FDG-labelled brine. Note that some snap shots are from time steps > 1 PV, i.e. after tracer break-through (visible from 1D profiles). Some development in saturation was seen after break-through, but flow remained concentrated in the outer circumference of the core

during displacement, and the core remained stable. The images on day 2, 3 and 4 show miscible traced brine-brine displacements in the core after overnight water injection following the first, second and third period of co-injection, respectively. The core is expected to be fully saturated by brine and dissolution is not expected during the miscible injections (no contrast in water chemistry between injected and displaced phase).

The F^{18}-FDG labelled brine saturation (Fig. 10) development was initially (day 1) piston-like in the inlet end of the core (until $x_D = 0.45$). In the remaining core the displacement mainly occurred in the outer part of the core circumference, leaving the core interior saturation static (no signal). The uneven displacement of traced water through the core could be related to internal heterogeneities in the core material. PET imaging verified that all traced brine signal remained in the porous medium. Note that a uniform tracer saturation was achieved in the core during two-phase co-injections- hence; the reactive flow was more evenly distributed in the core and not restricted to the edges, as shown in Supplementary Material C. Single–phase traced water injections clearly show the changes in flow patterns (and, hence, structure) in the core caused by dissolution. The breakthrough of traced water at the production end occurred earlier during miscible injections on day 2, indicating the formation of conductive pathways close to the core circumference. After the second (day 3 images) and third (day 4 images) period of co-injection the displacement pattern formed became more clear: the PET signal at the inlet end of the core plug becomes stronger, and a more dominant signal may be seen around the outer edge of the core circumference. Early breakthroughs at the production end compared to the initial displacement confirmed the formation of conductive pathways in the core. Signal
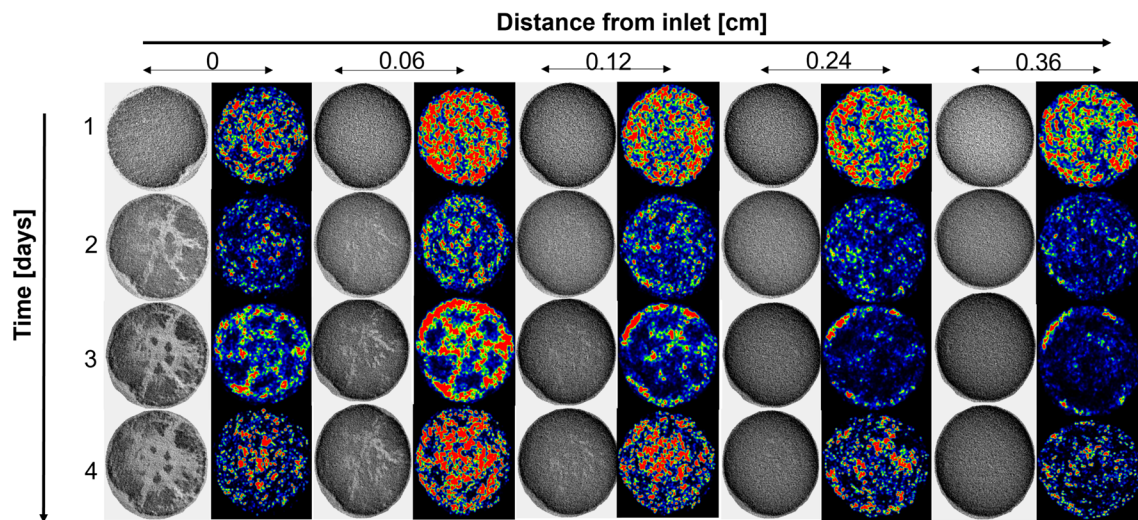
Fig. 11 Dissolution development for E-4 coreplug visualized by CT (grey-scale) and PET (RGB) imaging. The pattern of rock dissolution develops on the inlet end face and mimics the end piece distribution grooves: where a larger volume of fluid is available to interact with the rock. The pattern shape is maintained as the dissolution process spreads inwards. The color difference between days is not indicative of a saturation difference; but an artifact caused by slightly different tracer concentrations in the injected brine

Fig. 12 Regions of interest (ROIs) for PET analysis displayed at axial and coronal planes. The blue outer circunference indicates the intensity for the whole core and the red-dashed circunference shows the intensity in the middle of the coreplug
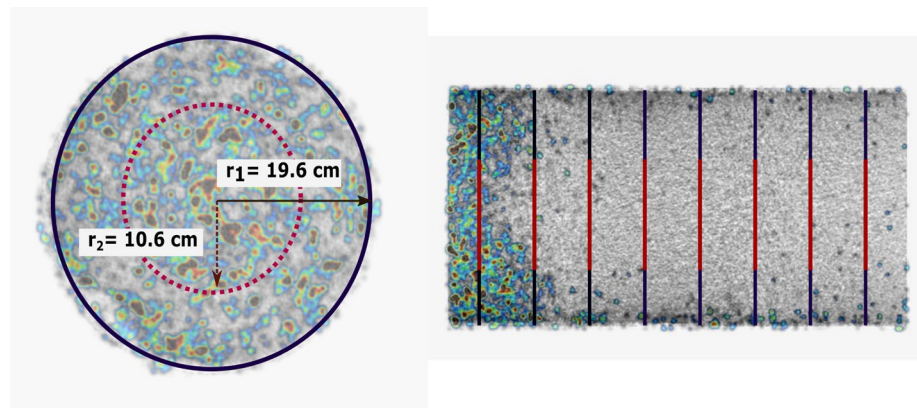

intensities for F^{18}-FDG labelled brine, l-CO_2 and two-phase injection (20% F^{18}-FDG labelled brine, 80% CO_2) during day 1–4 is available in Supplementary Material D–G.

Multi-modal CT and PET images of dissolution on Day 1–4 may be found in Fig. 11. Both imaging modalities were used to capture and confirm dissolution at five different positions close to the injection end. Rock dissolution first occurred on the inlet end face of the core and gradually moved inwards. CT images confirm that rock dissolution occurred by l-CO_2/brine co-injection; visible by dark areas in the CT image (low density area). The low density regions visible by CT coincide with a high PET signal: because the PET signal is produced by traced brine, a high signal is indicative of a higher volume of brine present, i.e. more voids, higher porosity or fluid in bulk. The images confirm that significant rock dissolution (CT: low signal intensity, PET: high signal intensity) occurs within the first 0.05 x_D of the core.

Local displacement variations were quantified on the sub-core scale. The PET images were sub-divided into two concentric shells for this analysis: one representing the center of the core and one the outer core edges (Fig. 12).

Figure 13 displays a snap shot of traced F^{18}-FDG brine saturation distribution at 0.5 PVI, and compares displacements pre-dissolution and after the first co-injection. Pre-dissolution the inner shell carries 27 % of the fluid for the first 0.3 x_D of the core. At 0.4 x_D core length 14 % of the fluids are displacing through the middle of the core, and the remaining through the outer edge. From 0.6 x_D the outer shell carries 95 % of flowing brine. After the first co-injection period significant changes in displacement distribution occurred: close to the injection end 29 % of

Fig. 13 Traced F^{18}-FDG brine saturation distribution at 0.5 PVI
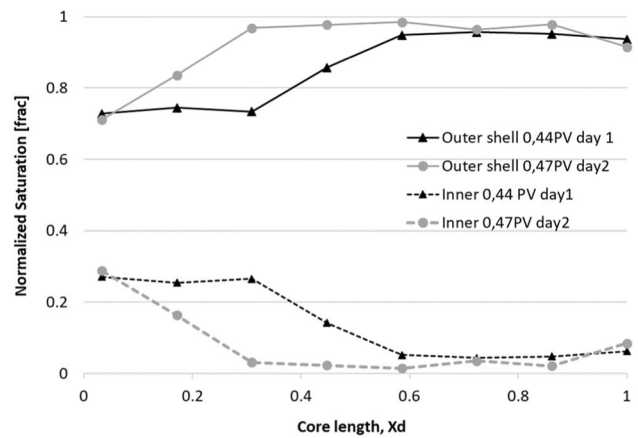
fluids were still flowing through the inner core- however, this quickly changed: at 0.2 x_D 84 % of the brine displaced through the outer core, and from $0.3x_D$ core length 97 % remained close to the core circumference. The outer core continue to conduct 97 % of flow from a core length of 0.3 x_D after the second and third period of co-injection. Fluid distribution, however, changed close to the inlet end after all three periods of co-injections due to dissolution: on day 4 the inner part of the core carried 41 % of the fluid close to the inlet (0.03 x_D) and 28 % of the fluid flow at 0.17 x_D. The high volume of fluid in the inner part of the core this close to the inlet is caused by the developed dissolution pattern (Fig. 11).

The dynamic fluid distribution development as a function of injected volume and dissolution (time) is shown in Fig. 14. Traced brine flows through both the inner and outer part of the core pre-dissolution and after the first period of co-injection. After the second period of co-injection, however, less brine is displaced through the inner segment of the core and the preferred flow path swiftly shifts to the outer core. After the third period of co-injection very little brine
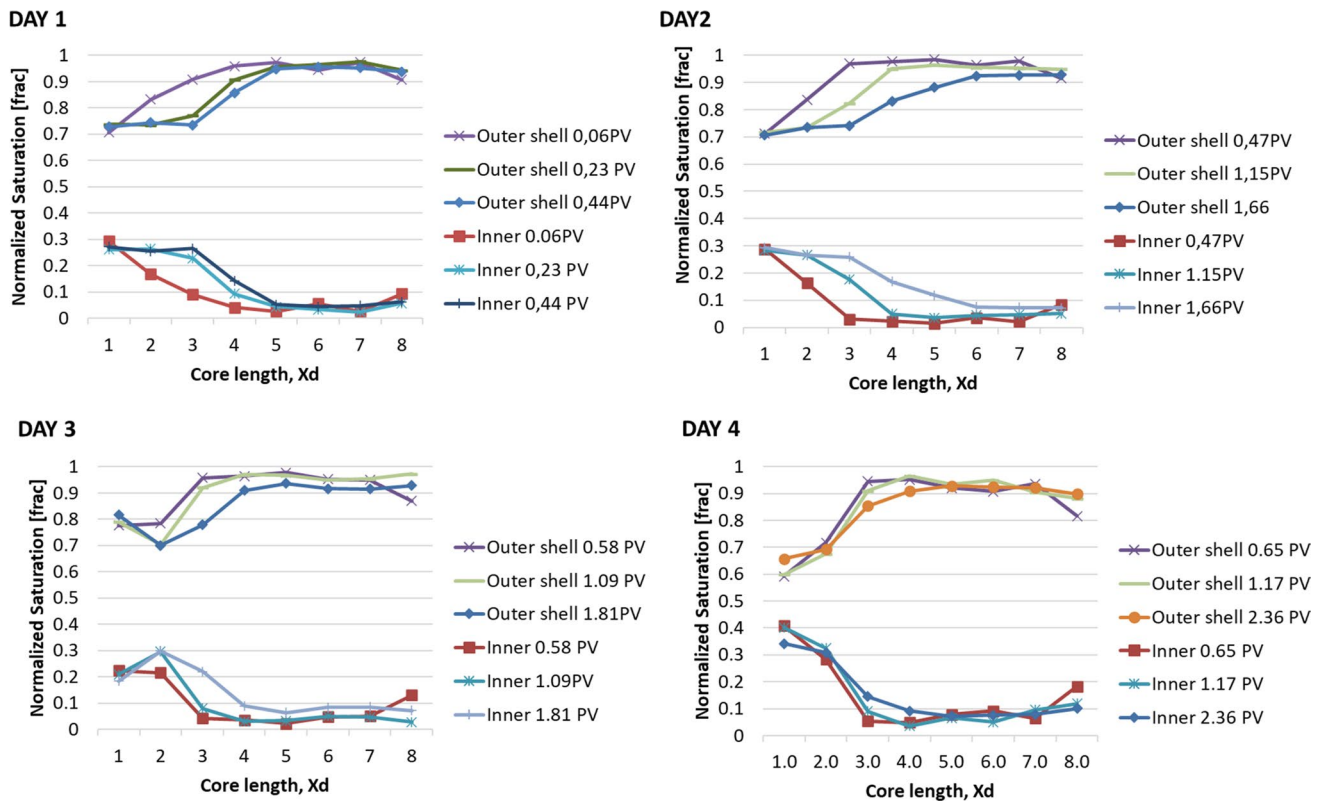
Fig. 14 Dynamic fluid distribution development as a function of injected volume and dissolution per day

moves through the inner core part: the signal is high close to the inlet due to the dissolution pattern, which provides storing for bulk fluid close to the end piece. The flowing fluids immediately move out from the inner core area to flow in the preferential flow paths close to the core circumference.

The non-uniform displacements visualized at core scale were confirmed at sub-core scale, and may initially be associated with a heterogeneous rock pore structure. During co-injections the displacement of reactive fluid was more uniform. Rock dissolution was confirmed close to the inlet and has likely also occurred internally in the core. The dissolved rock material is carried with the flowing fluids into the core interior and may have deposited to block pore throats within the core. In three of four core floods in this work the absolute core permeability decreased after brine and CO_2 co-injections. Izgec et al. [37] also reported a permeability reduction when CO_2 was injected into heterogeneous Midyat cores, and attributed the change to an uneven pore size distribution that rendered the deposition of calcite particles along the possible flow paths. Mangane et al. [38] also observed a significant clogging of macropores that resulted in a permeability decrease when a CO_2-enriched brine was injected into a limestone coreplug. The dominant mechanism for the permeability impairment was found to be the formation of microporous material due to the dissolution of microcrystaline cement. In core E-4 absolute permeability increased (Table 8). Imaging during traced brine injections, however, show that that brine preferentially moved along the outer edge of the core, and consequently global pressure measurements mainly captured the permeability development here.

3.3 Dissolution at multiple-scales

In this work we aim to further the understanding of calcite dissolution during carbon sequestration at multiple scales. Micro-scale Isothermal Titration Calorimetry (ITC) is a robust technique that gives a direct appraisal of the thermodynamics behind a binding interaction. By measuring heat it is possible to obtain the enthalpy of the interaction, which makes ITC a unique method to obtain the adsorption energy in comparison to other alternatives based on theoretical calculations (e.g. van't Hoff method). Rock dissolution can be obtained by analyzing the composition of the rock and fluids by different methods used in analytical chemistry (e.g. ICP-OES for changes in the brine composition and XRF for changes in the rock composition). However, these methods are only complementary to ITC; which is currently the only method that can measure interfacial interactions between rocks and fluids. Hence, ITC may be a valuable addition to the experimental CCS tool box, that is currently focused on mineralogical changes after dissolution, and not dynamically occurring interactions. ITC experimentally verified that the rock–brine system becomes more reactive when CO_2 is present: at both microscopic and macroscopic core scale. Core scale experiments with the same core material and fluid/rock systems confirmed that dissolution of rock material occurred during two–phase injections (CO_2 available), while the rock material remains stable during single phase brine–injections. Our macroscopic measurements emphasize that complex pore structures also controls dissolution: by distributing the availability and ratio of reactive fluid non-uniformly throughout the porous medium. Both microscopic interactions and reactive flow heterogeneity will ultimately control dissolution at relevant storage scale. The synergy between microcalorimetry experiments and core floods can aid the understanding of CO_2/rock/brine interactions and the impact on flow, but cannot capture the complexity of larger carbonate formations. Using and further developing new multi-scale methodology may, however, provide insight into the interplay between several controlling parameters for carbon sequestration. Future multi–scale studies may include the influence of heterogeneous pore structure and mineralogy, salinity and mixing processes occurring when injected fluids come in contact with reservoir fluids; which remain useful at various storage conditions.

4 Conclusions

This work presented a novel synergy between microcalorimetry and core flooding experiments to evaluate rock dissolution. Visualization and sub-core quantification by PET/CT imaging support our conclusions:

- Fluid-fluid interactions indicate that the presence of CO_2 causes a large perturbation in the hydrogen bonding between the water molecules (water-water network)
- The results from the Isothermal Titration Calorimetry (ITC) indicated that entropy drives dissolution process, which is unfavourable with respect to enthalpy change but thermodynamically favorable with respect to entropy change (cations and hydrogen carbonate concentrations increase in the brine).

- The steady-state co-injection of a NaCl brine and CO_2 at supercritical and liquid conditions causes a non-continuous dissolution of Edwards Limestone.
- The heat absorbed by limestone+NFB+B_{CO_2} is higher than for limestone+NFB+ NaCl brine, showing that CO_2 makes the injected fluid more reactive with the rock+fluid system.
- The overall permeability reduction measured during continuous co-injection at the core scale can be attributed to calcite precipitation inside the porous medium, which was higher for the first 100 PVI at both supercritical and liquid conditions.
- Microscopically, the dissolution rate using l-CO_2/NaCl brine is slightly higher than for sc-CO_2/NaCl for this rock material. This could be associated with a higher amount of CO_2 moles present at the liquid CO_2-brine interface and therefore also at the rock-liquid interface- resulting in more dissolution of the rock minerals.
- The rock dissolution was identified by a low signal density in computed tomography (CT) and high signal density in positron emission tomography (PET).
- PET/CT imaging shows a non-uniform dissolution of Edwards Limestone which results from heterogeneities in the porous medium (variations in the reactive fluid flow).
- The rock-brine system becomes more reactive when CO_2 is present at both microscopic and macroscopic core scales.

Data availability The datasets are available from the corresponding author on reasonable request.

References

1. Metz B, Davidson O, De Coninck H, Loos M, Meyer L. IPCC special report on carbon dioxide capture and storage. Cambridge: Cambridge University Press; 2005.
2. Centre for Science and Environment. Ipcc's special report on global warming of 1.5°c: Assessment and recommendations. Tech. Rep., Centre for Science and Environment (2018). http://www.jstor.org/stable/resrep37860.
3. Dincer I, Colpan C, Kadioglu F. Causes, impacts and solutions to global warming. New York: Springer; 2013.
4. IEA. Global energy review 2021. Tech. Rep., IEA (2021). https://www.iea.org/reports/global-energy-review-2021.
5. Al-Khdheeawi EA, Vialle S, Barifcani A, Sarmadivaleh M, Iglauer S. Enhancement of CO_2 trapping efficiency in heterogeneous reservoirs by water-alternating gas injection. Greenh Gas Sci Technol. 2018;8(5):920–31.
6. Motie M, Assareh M. CO_2 sequestration using carbonated water injection in depleted naturally fractured reservoirs: a simulation study. Int J Greenh Gas Control. 2020;93: 102893. https://doi.org/10.1016/j.ijggc.2019.102893.
7. Cobos JE, Kissami Y, Alkutaini IA, Søgaard EG. Microcalorimetric study of carbonating produced water as a promising CO_2 storage and enhanced oil recovery method. Energies. 2022. https://doi.org/10.3390/en15082888.
8. Sohal MA, Thyne G, Søgaard EG. Review of recovery mechanisms of ionically modified waterflood in carbonate reservoirs. Energy Fuels. 2016;30(3):1904–14. https://doi.org/10.1021/acs.energyfuels.5b02749.
9. Yuan T, Ning Y, Qin G. Numerical modeling and simulation of coupled processes of mineral dissolution and fluid flow in fractured carbonate formations. Transport Porous Media. 2016;114(3):747–75.
10. Hao Y, Smith MM, Carroll SA. Multiscale modeling of CO_2-induced carbonate dissolution: from core to meter scale. Int J Greenh Gas Control. 2019;88:272–89. https://doi.org/10.1016/j.ijggc.2019.06.007.
11. *Carbon Dioxide - Dolomite Rock Interaction During* CO_2 *Flooding Process*, Vol. All Days of *PETSOC Annual Technical Meeting*. https://doi.org/10.2118/83-34-17.
12. Kaufmann G, Dreybrodt W. Calcite dissolution kinetics in the system $CaCO_3$-H_2O-CO_2 at high undersaturation. Geochimica et Cosmochimica Acta. 2007;71(6):1398–410. https://doi.org/10.1016/j.gca.2006.10.024.
13. CO_2 *Injection in Carbonates*.
14. Coto B, Martos C, Peña J, Rodríguez R, Pastor G. Effects in the solubility of $CaCO_3$: experimental study and model description. Fluid Phase Equilib. 2012;324:1–7. https://doi.org/10.1016/j.fluid.2012.03.020.
15. Luquot L, Rodriguez O, Gouze P. Experimental characterization of porosity structure and transport property changes in limestone undergoing different dissolution regimes. Transport Porous Media. 2014;101(3):507–32.

16. Smith M, Hao Y, Carroll S. Development and calibration of a reactive transport model for carbonate reservoir porosity and permeability changes based on CO_2 core-flood experiments. Int J Greenh Gas Control. 2017;57:73–88. https://doi.org/10.1016/j.ijggc.2016.12.004.

17. Menke H, et al. 4d multi-scale imaging of reactive flow in carbonates: assessing the impact of heterogeneity on dissolution regimes using streamlines at multiple length scales. Chem Geol. 2018;481:27–37. https://doi.org/10.1016/j.chemgeo.2018.01.016.

18. Graue A, Viksund BG, Baldwin BA. Reproducible wettability alteration of low-permeable outcrop chalk. SPE Reserv Eval Eng. 1999;2(02):134–40. https://doi.org/10.2118/55904-PA.

19. Housecroft C, Sharpe A. Inorganic chemistry. London: Pearson Education Limited; 2005.

20. National Institute of Standards and Technology. US Department of Commerce. Thermophysical Properties of Fluid Systems. https://webbook.nist.gov/chemistry/fluid/ (2022). Accessed: 2022-01-13.

21. Tipura, L. *Wettability Characterization by NMR T2 Measurements in Edwards Limestone*. Master's thesis, University of Bergen, Department of Physics and Technology (2008).

22. Folkvord, O. *Applying in-situ imaging and streamtube analysis to quantify carbonate dissolution at the core scale – an experimental study applying positron emission tomography (PET) and computed tomography (CT)*. Master's thesis, University of Bergen, Department of Physics and Technology (2021).

23. Cobos JE, Westh P, Søgaard EG. Isothermal titration calorimetry study of brine oil rock interactions. Energy Fuels. 2018;32(7):7338–46. https://doi.org/10.1021/acs.energyfuels.8b00512.

24. Cobos JE, Søgaard EG. Effect of individual ions on rock-brine-oil interactions: a microcalorimetric approach. Fuel. 2021;290: 119955. https://doi.org/10.1016/j.fuel.2020.119955.

25. Cobos JE, et al. Evaluation of wettability alteration in heterogeneous limestone at microscopic and macroscopic levels. J Petrol Sci Eng. 2021;202: 108534. https://doi.org/10.1016/j.petrol.2021.108534.

26. *Of rats and rocks: using pre-clinical PET imaging facilities in core analysis*, Vol. 366 of *The 35th International Symposium of the Society of Core Analysts*. url = https://doi.org/10.1051/e3sconf/202336601011.

27. Cobos JE, Søgaard EG. Impact of compositional differences in chalk and water content on advanced water flooding: a microcalorimetrical assessment. Energy Fuels. 2020;34(10):12291–300. https://doi.org/10.1021/acs.energyfuels.0c02108.

28. Cobos JE, Søgaard EG. Systematic study of geothermal brine reinjection for saltpower generation purposes: citric acid as a potential iron control agent. Geothermics. 2021;95: 102116. https://doi.org/10.1016/j.geothermics.2021.102116.

29. Cobos JE, Søgaard EG. Study of geothermal brine reinjection by microcalorimetry and core flooding experiments. Geothermics. 2020;87: 101863. https://doi.org/10.1016/j.geothermics.2020.101863.

30. Lasaga AC. Chemical kinetics of water-rock interactions. J Geophys Res Solid Earth. 1984;89:4009–25. https://doi.org/10.1029/JB089iB06p04009.

31. Golfier F, et al. On the ability of a darcy-scale model to capture wormhole formation during the dissolution of a porous medium. J Fluid Mech. 2002;457:213–54. https://doi.org/10.1017/S0022112002007735.

32. Stipp SL, Hochella MF. Structure and bonding environments at the calcite surface as observed with x-ray photoelectron spectroscopy (xps) and low energy electron diffraction (leed). Geochim et Cosmochim Acta. 1991;55(6):1723–36. https://doi.org/10.1016/0016-7037(91)90142-R.

33. Van Cappellen P, Charlet L, Stumm W, Wersin P. A surface complexation model of the carbonate mineral aqueous solution interface. Geochim et Cosmochim Acta. 1993;57(15):3505–18. https://doi.org/10.1016/0016-7037(93)90135-J.

34. Stipp S, Eggleston C, Nielsen B. Calcite surface structure observed at microtopographic and molecular scales with atomic force microscopy (afm). Geochimica et Cosmochimica Acta. 1994;58(14):3023–33. https://doi.org/10.1016/0016-7037(94)90176-7.

35. Du Z, de Leeuw NH. Molecular dynamics simulations of hydration, dissolution and nucleation processes at the alpha-quartz (0001) surface in liquid water. Dalton Trans Int J Inorg Chem. 2006;22:2623–34.

36. Liu Z, Yuan D, Dreybrodt W. Comparative study of dissolution rate-determining mechanisms of limestone and dolomite. Environ Geol. 2005;49(2):274–9.

37. Izgec O, Demiral B, Bertin H, Akin S. CO_2 injection into saline carbonate aquifer formations ii: comparison of numerical simulations to experiments. Transport Porous Media. 2007;73(1):57–74.

38. Mangane PO, Gouze P, Luquot L. Permeability impairment of a limestone reservoir triggered by heterogeneous dissolution and particles migration during co_2-rich injection. Geophys Res Lett. 2013;40(17):4614–9. https://doi.org/10.1002/grl.50595.

39. Snippe J, Berg S, Ganga K, Brussee N, Gdanski R. Experimental and numerical investigation of wormholing during CO_2 storage and water alternating gas injection. Int J Greenh Gas Control. 2020;94: 102901.